

RESEARCH ARTICLE

Transport Phenomena and Fluid Mechanics

Four stages of thermal effect coupled with ion-charge transports during the charging process of porous electrodes

Pan Huang¹ | Haolan Tao¹ | Jie Yang² | Cheng Lian^{1,2}  | Honglai Liu^{1,2}

¹State Key Laboratory of Chemical Engineering, Shanghai Engineering Research Center of Hierarchical Nanomaterials, School of Chemical Engineering, East China University of Science and Technology, Shanghai, People's Republic of China

²School of Chemistry and Molecular Engineering, East China University of Science and Technology, Shanghai, People's Republic of China

Correspondence

Cheng Lian, School of Chemistry and Molecular Engineering, East China University of Science and Technology, Shanghai 200237, People's Republic of China.

Email: liancheng@ecust.edu.cn

Funding information

Jiangsu Engineering Laboratory of New Materials for Sewage Treatment and Recycling; The National Natural Science Foundation of China, Grant/Award Numbers: 22078088, 91834301; The National Natural Science Foundation of China for Innovative Research Groups, Grant/Award Number: 51621002; The Shanghai Rising-Star Program, Grant/Award Number: 21QA1401900

Abstract

Due to the complexity of thermal effects in porous electrodes, the process of temperature rise in supercapacitors is difficult to be quantified by some simple but physically meaningful formulas. Here, the stack-electrode model is applied to investigate this issue both analytically and numerically. The numerical results show the process has three relaxation times, which divide that into four stages controlled by heat generation (HG) or heat transfer (HT). Temperature rise is first controlled by HG in the bulk phase, then by HG in both porous electrodes and bulk phase, then mainly by HT, and finally all by HT. The analytical formulas of three relaxation times and temperature rise under different structural parameters and intensity of heat dissipation are obtained. These formulas are expected to indicate the contribution of the different stages to total temperature rise, thus to guide the design of cooling methods of supercapacitors during the different stages.

KEY WORDS

ion transport, porous electrode, relaxation time, temperature rise, thermal effect

1 | INTRODUCTION

Supercapacitors have attracted tremendous attention due to rapid charging and discharging, highly prolonged cycle life, and excellent stability compared with batteries,^{1,2} showing great potential for the green grid,³ portable electronics,⁴ and especially hybrid vehicles.^{1,5,6} In these typical commercial applications, supercapacitors are charged and discharged at a very high current rate either for vehicle acceleration or for braking energy recuperation, producing a large amount of volumetric heat in a very short time that dramatically increases the temperature of supercapacitors.^{7,8} An over-high temperature will lead to the increase of capacitance internal pressure, the aging of the collector, thus the increase of self-discharge rates, and then the shortening of cycle life.^{7,9,10} Eventually, the supercapacitors will be destroyed

and even exploded due to the evaporation and expansion of electrolytes under excessive temperature without any heat dissipation, inducing safety problems.^{9,11} Consequently, deeply understanding the thermal effect, especially quantizing the process of temperature rise using simple formulas, and hence performing rational thermal management are key issues concerning the performance, lifetime, and safety of supercapacitors.^{12,13}

Due to confinement effects,^{14,15} porous electrodes, especially amorphous carbon electrodes,^{1,2} possess a denser packing of the ions inside the pores compared with planar electrodes, resulting in a higher capacitance and wider applications. However, porous electrodes also lead to more heat generation (HG) and thus more insecurity. Besides, the complex geometry of porous electrodes brings two more issues when studying the thermal effects than planar electrodes. As shown in Figure 1A, during the charging process, ions in the bulk phase are driven toward and adsorbed on the surface of the micro-scale, even

Pan Huang and Haolan Tao contributed equally to this work.

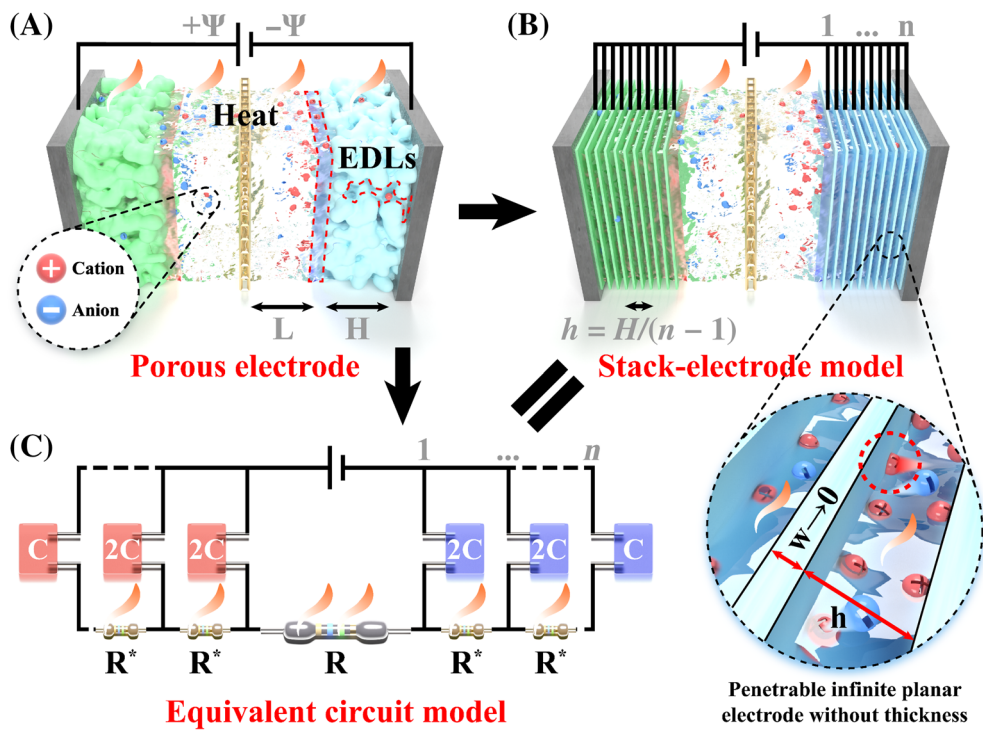


FIGURE 1 The supercapacitor with porous electrodes and its simplified simulation models. (A) The sketch of a supercapacitor containing a 1:1 electrolyte and two porous electrodes, and a battery providing an electrostatic potential difference 2Ψ . (B) In the one-dimensional stack-electrode model, the cathode and anode each contain n infinite planar electrodes at intervals of h . Initial anionic and cationic densities are ρ_{bulk} throughout the cell. At time $t=0$, $+\Psi$ and $-\Psi$ are applied to all electrodes on the left and right-hand sides of the system, respectively. The zoom-in view of the interface of electrode and electrolyte indicates that the planar electrode is infinite and has no thickness. Notably, it is assumed that every electrode has penetrable zones except for the outmost one and the ions can pass through them. (C) The equivalent circuit model (ECM) for the one-dimensional stack-electrode model

nano-scale pores in porous electrodes by electrostatic interaction, to produce current and to form electrical double layers (EDLs) in both the bulk phase and the porous electrodes. Therefore, the first issue is how to describe the thermal effect in porous electrodes, which is affected by a complex coupling of confinement effect, migration of ions, heat transfers (HTs), and the formation of EDLs.^{16–18} What's more, the model should also consider the thermal effect in the bulk phase and the connection with that in porous electrodes. The second issue is how to obtain some simple formulas with physic meanings to describe the process of temperature rise in porous electrodes, so as to scientifically guide the establishment of a thermal management system of supercapacitors. For the planar supercapacitor, the relaxation time of HG derived by the equivalent circuit model (ECM) and that of HT¹⁸ can quantitatively divide the process of temperature rise into three stages. The temperature rise during three stages can be also obtained. However, ECM hardly describes the irregular structure of amorphous carbon electrodes.

At present, in contrast to experimental methods, such as isothermal calorimeters,¹² accelerated rate calorimeter,¹³ and miniature resistance temperature detector (RTD) Sensor,¹⁹ the simulation techniques provide effective alternatives to study the multiphysical field coupling thermal effect and to measure the temperature rise in the porous electrodes *in situ*.²⁰ Among the commonly used simulation techniques, the continuum models^{21–23} are faster than all atoms/coarse-grained molecular dynamics simulations^{24,25} and are more accurate than

ECM^{26,27} at simulating the charging dynamics and temperature rise of mesoscale system containing the bulk phase and porous electrodes. The continuum model describes the evolution of ion concentration, potential, and temperature by partial differential equations (PDEs), such as Poisson-Nernst-Planck (PNP) equations, with given initial and boundary conditions.²⁸ However, for amorphous carbon electrodes shown in Figure 1A, the boundary conditions are particularly complicated due to irregular surface structure and the difference of spatial scale between pore and bulk phase, leading to the time-consuming of solving the PNP equations.^{29,30} Therefore, a variety of empirical models or simplified geometric models of amorphous carbon electrodes have been proposed. The equivalent porous medium models of thermal effect in supercapacitors^{7,8,10} were first proposed to predict the temperature distribution within a cell by solving the modified energy equation with equivalent thermal conductivity. Nevertheless, equivalent porous medium model ignores the microstructure of electrodes. Then, Newman et al.^{31,32} develop the pseudo two-dimensional (P2D) model to study charging process³³ and thermal effect³⁴ of lithium ion battery. P2D model simulates the intercalation/deintercalation process by assuming active material as isotropic spherical particles of uniform size. Meanwhile, Bazant et al.³⁵ presented a novel porous electrode theory to describe the predominantly bimodal distribution of pores consists of the macropores outside the particles and the micropores inside the particles, which has been applied to

capacitive deionization,^{21,36,37} salinity gradient power generation³⁸ and electrochemical systems.³⁹ However, these abovementioned models employ the volume averaging method to simplify the structural complexities and introduce volume fraction and tortuosity as two effective structural descriptors rather than exact multiscale geometrical detail.^{40,41} Fractal dimension is an alternative to represent the geometrical detail. Recently, Huang⁴⁰ studied the impedance response of a porous electrode with a fractal microscopic pore structure by solving fractional PDEs. However, fractional PDEs are hard to be solved analytically than integer order PDEs, and the only way to get relaxation time is to fit the numerical solutions, which has limited applicability and less physical significance. Therefore, a simplified model representing both complex microstructure of amorphous carbon electrodes and macrostructure of the bulk phase is in urgent demand, with which the analytical formulas of relaxation time and temperature rise in the charging and temperature rise processes are expected to be derived. More recently, Lian et al.²³ have proposed a novel, simple and physics-based stack-electrode model to represent the porous electrode and bulk phase, and successfully explained the slow charging dynamics of supercapacitors with amorphous carbon electrodes by the PNP equations and the ECM. Besides, they derived the formulas of relaxation times of surface charge and found the charging process can be divided into three stages by two relaxation times, which has been observed in the experimental data.¹³ Whereafter, Lin et al.⁴² applied the stack-electrode model to the cyclic voltammetry in porous electrodes.

In this work, we utilize the stack-electrode model to simplify amorphous carbon electrodes and study the thermal effect in supercapacitor by ECM, and the PNP and heat equations, as shown in Figure 1. Simple formulas with physical meanings of relaxation times τ and adiabatic temperature rise ΔT_{eq} in porous electrode are first

analytically derived by ECM. Then, the ion-charge-heat coupled numerical simulations based on the PNP and heat equations are implemented to find the number of stages of temperature rise characterized by τ . Meanwhile, the effects of HG and HT on every stage of temperature rise in the bulk phase and porous electrodes are revealed. Then, we discuss the roles of structural parameters on τ , ΔT_{eq} , and temperature rise at the end of every stage ΔT_τ , simultaneously verify and optimize these formulas derived by ECM. Finally, the influences of heat dissipation are studied to lay the foundation of thermal management of supercapacitors with porous electrodes.

2 | METHODOLOGY

2.1 | The stack-electrode model

2.1.1 | The simplification process of amorphous carbon electrode structure

Figure 2 shows the simplification process from two-dimension amorphous carbon electrode to one-dimension stacked planar electrodes. Figure 2A,B is planar electrode and amorphous carbon electrode, respectively. Notably, the thickness of amorphous carbon electrode is H and the pore size r is uniform. Electronic connections through the electrode (drawn as black lines) allow for the injection of charge from an external circuit.²¹ Figure 2C is an ideal cell model⁴³ constructed by an array of square electrodes (i.e., carbon particle in Figure 2B) with side length w . To make the next simplification process easier to understand, the gaps along y direction are named by permeable zones and colored by gray, as shown in Figure 2D. Because the porous electrode is infinitely large along y direction and all ions are ideal point charge, we

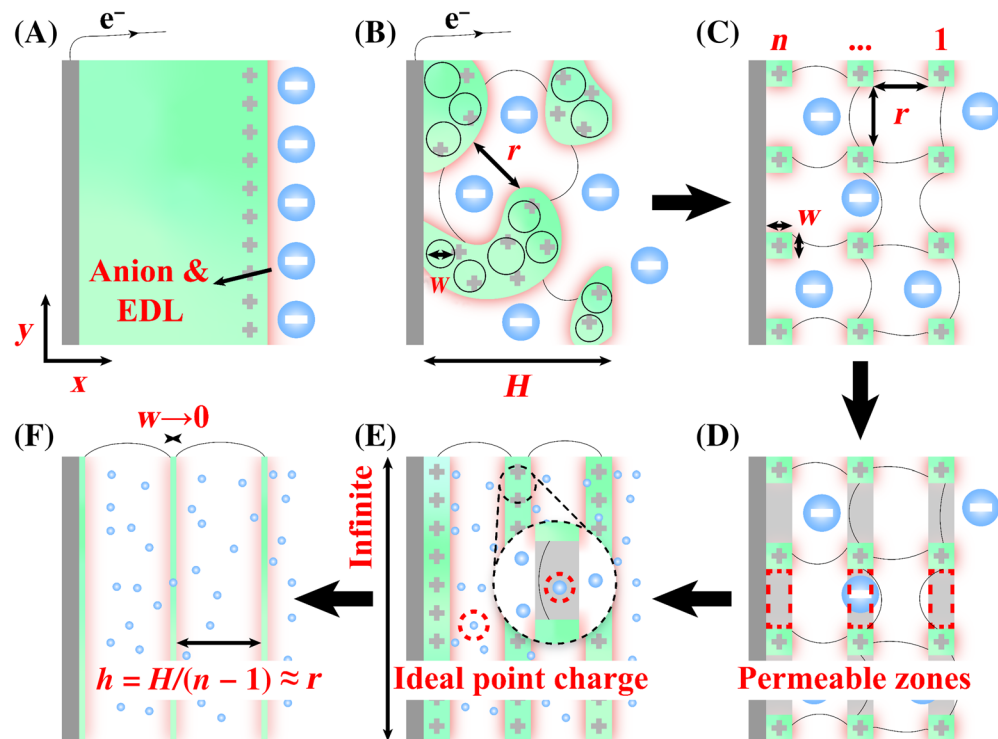


FIGURE 2 (A) Planar electrode and the simplification process from (B) amorphous carbon electrode with uniform pore size to (C) ideal cell model to (D) ideal cell model with permeable zones to (E) stacked planar electrodes with thickness to (F) stacked planar electrodes without thickness

assume that the square electrodes along y direction are macroscopically connected to form a planar electrode of thickness w but microscopically separated by permeable zones, as shown in Figure 2E. The influence of w on charging dynamics is ignored if porosity tends to 1 (i.e., $w \ll r$). Figure 2F presents the final simplified model of amorphous carbon electrode in this work, where the number of planar electrodes is n and the interlayer spacing of adjacent planar electrodes is h . The simplified model can reflect the key properties of porous electrode and can be solved quickly.

All assumptions of simplification process and their reasonableness are listed in Section S2. These assumptions will be relaxed in future studies.

2.1.2 | The physical meanings of structure parameters

The pore size r can be measured by Brunauer-Emmett-Teller (BET) and the ratio of carbon particle size w to r can be obtained from SEM image. n is the number of planar electrodes and related to r and w , that is $n = (H+r)/(w+r)$, where H is the thickness of electrode. So, n is like an index for indicating the depth of the pore. Meanwhile, $H = (n-1)h$, where h is the interlayer spacing of adjacent planar electrodes. Therefore, the relation between h and r is $h = n/(n-1)w + r$. If $w \ll r$ (porosity tends to 1), $h \rightarrow r$. So, h could moderately represent the pore size of amorphous carbon electrode r , which can be adjusted by n and H .

2.1.3 | Charging process

A simplified one-dimensional stack-electrode model of supercapacitor with porous electrodes²³ is introduced in Figure 1B, containing a 1:1 electrolyte and stacked planar electrodes separated by a distance $2L$. In the layered electrode structure, both cathode and anode are composed of n planar electrodes with no thickness, as shown in Figure 2F. Once the potential difference 2Ψ is applied by battery, electrons are transferred to the surface of the planar electrode by the black lines, leading to an electric field. The opposite ions from the bulk phase are driven to counter the inside planar electrode through permeable zones, subsequently forming the EDLs near all the planar electrodes. The equilibrium thickness of the EDL is characterized by the Debye length $\lambda_D = \kappa^{-1} = \sqrt{(\epsilon_0 \epsilon_r k_B T_0) / (2e^2 \rho_{\text{bulk}})}$, with ϵ_0 the vacuum permittivity, ϵ_r the relative permittivity of electrolyte, k_B the Boltzmann constant, T the temperature, e the elementary charge, and ρ_{bulk} the bulk ionic number density.

2.2 | Analytic method: Equivalent circuit model

To give an accurate description of the influence of these structural parameters and operating conditions in the stack-electrode model on

thermal effect, an ECM is introduced, as shown in Figures 1C and 3. The capacitor represents the energy storage capacity of EDL and the resistor represents the resistance of electrolyte in nanopores and the bulk phase. Notably, ECM can only simulate HG in supercapacitors. The capacitance of the outmost capacitor is C because only one side contacts with electrolyte.

2.2.1 | $n = 1$ case

The planar supercapacitors can be described by the circuit model of trivial $n = 1$ case shown in Figure 3A. Interfacial charge storage at the EDL is C and the ion transport resistance through the electrolyte is R . Once a potential difference 2Ψ is applied at $t = 0$, the capacitor will acquire a time-dependent charge $Q(t) = C\varphi(t)$, where $\varphi(t)$ is the time-dependent voltage difference between either side of the capacitors. The current I that flows through the system is found via Ohm's law, $IR = [\Psi - \varphi(t)] - [-\Psi + \varphi(t)] = 2[\Psi - \varphi(t)]$. With $I = \dot{Q}(t) = C\dot{\varphi}(t)$, we get $\dot{\varphi} = 2[\Psi - \varphi(t)]/(RC)$. For $\varphi(t=0) = 0$, the $\varphi(t)$ can be expressed as:

$$\varphi(t) = \Psi \left[1 - \exp \left(-\frac{2t}{RC} \right) \right]. \quad (1)$$

Since the EDL capacitance $C = A\epsilon_0 \epsilon_r \kappa$ and electrolyte resistivity $R = 2L/(A\epsilon_0 \epsilon_r \kappa^2 D)$ with A the surface area facing the electrolyte and D the ion diffusivity, we can find $RC = 2L\kappa^{-1}/D = 2\tau_{RC}$, where the relaxation time of the RC circuit²³ $\tau_{RC} = L\kappa^{-1}/D$. Therefore, the relaxation time of surface charge $\tau_\sigma = RC/2 = \tau_{RC}$.

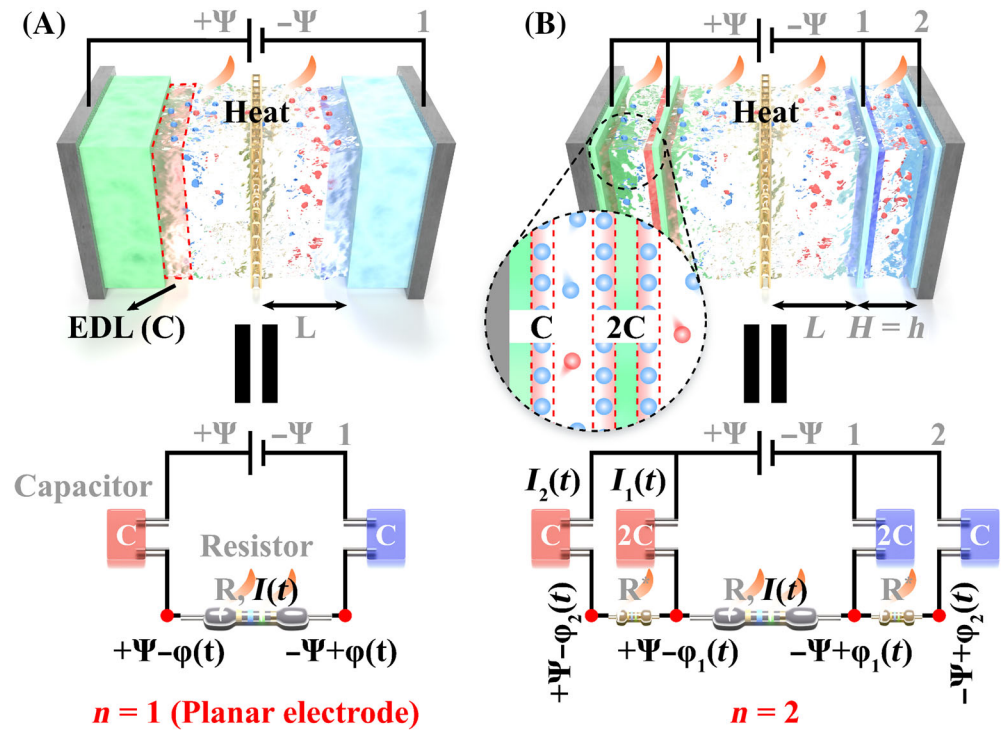
Assuming the capacitor does not generate heat, and Joule heat generated by the resistor is the only source of heat, then the HG power P_0 of the circuit is:

$$P_0 = \frac{[(\Psi - \varphi(t)) - (-\Psi + \varphi(t))]^2}{R} = \frac{4\Psi^2}{R} \exp \left(-\frac{4t}{RC} \right), \quad (2)$$

$$\begin{aligned} \frac{\partial T}{\partial t} &= \frac{\partial(T - T_0)}{\partial t} \\ &= \frac{P_0}{\rho_{m,\text{bulk}} c_p [2(H+L)A]} \\ &= \frac{\epsilon \kappa^4 D}{\rho_{m,\text{bulk}} c_p} \frac{\Psi^2}{(1 + \frac{H}{L})^2 (\kappa L)^2} \exp \left(-\frac{4t}{RC} \right), \end{aligned} \quad (3)$$

$$\begin{aligned} \Delta T_0 &= T - T_0 = \int_0^t \frac{\partial T}{\partial t} dt \\ &= \frac{\epsilon \kappa^2}{2\rho_{m,\text{bulk}} c_p} \frac{\Psi^2}{(1 + \frac{H}{L})^2 \kappa L} \left[1 - \exp \left(-\frac{4t}{RC} \right) \right] \\ &= T_{\text{eq}} \left[1 - \exp \left(-\frac{4t}{RC} \right) \right], \end{aligned} \quad (4)$$

FIGURE 3 The equivalent circuit models (ECM) for the stack electrode model in the trivial cases (A) $n = 1$ and (B) $n = 2$



where T_0 is the initial temperature and T_{eq} is the adiabatic temperature rise at equilibrium. Therefore, the relaxation time of HG is:

$$\tau_g = \tau_{g,0} = RC/4 = L\kappa^{-1}/(2D) = 0.5\tau_{RC}. \quad (5)$$

2.2.2 | $n = 2$ case

For $n = 2$, the outer capacitors ($i = 2$) have a capacitance C , while inner capacitors ($i = 1$) have $2C$, because inner planar electrodes are facing the electrolyte twice, as shown in Figure 3B. The electrolyte resistivities in the bulk phase and pore are $R = 2L/(A\varepsilon_0\varepsilon_r\kappa^2 D)$ and $R^* = H/(A\varepsilon_0\varepsilon_r\kappa^2 D)$, respectively. Hence, $R^*/R = H/(2L)$ and $RC = 2\kappa^{-1}L/D$. Lian et al.²³ have successfully solved the matrix formula for the voltage difference between either side of the capacitor $\varphi_i(t)$. Here, we rederive the full formula for $\varphi_i(t)$, following the above procedure of $n = 1$:

$$\begin{aligned} \varphi_1(t) &= \frac{H(u_{11}u_{22}B_1 - u_{12}u_{21}B_2)}{L(u_{11}u_{22} - u_{12}u_{21})}\Psi \text{ and} \\ \varphi_2(t) &= \frac{H(u_{21}u_{22}B_1 - u_{22}u_{21}B_2)}{L(u_{11}u_{22} - u_{12}u_{21})}\Psi, \end{aligned} \quad (6)$$

$$B_1 = \left[1 - \exp\left(-\frac{\lambda_1 t}{2R^*C}\right)\right] \frac{1}{\lambda_1} \text{ and } B_2 = \left[1 - \exp\left(-\frac{\lambda_2 t}{2R^*C}\right)\right] \frac{1}{\lambda_2}, \quad (7)$$

$$\lambda_1, \lambda_2 = \text{eig}(\vec{M}) \text{ and } M = \frac{1}{2R^*C} \begin{pmatrix} 1 + 2R^*/R & -1 \\ -2 & 2 \end{pmatrix}, \quad (8)$$

where $u_{21}/u_{11} = 1 + H/L - \lambda_1$, $u_{22}/u_{12} = 1 + H/L - \lambda_2$, λ_1 , and λ_2 are the eigenvalues of the matrix M .

The HG powers in the bulk phase P_0 and in the pore P_{12} are:

$$\begin{aligned} P_0 &= \frac{4H^2}{L^2} F^2 \frac{\Psi^2}{R} \left[\left(\frac{L}{HF} - \frac{G_{11}}{\lambda_1} - \frac{G_{12}}{\lambda_2} \right) + \frac{G_{11}}{\lambda_1} \exp\left(-\frac{L\lambda_1 t}{HRC}\right) \right. \\ &\quad \left. + \frac{G_{12}}{\lambda_2} \exp\left(-\frac{L\lambda_2 t}{HRC}\right) \right]^2, \end{aligned} \quad (9)$$

$$P_{12} = \frac{2H}{L} F^2 \frac{\Psi^2}{R} \left[\left(\frac{G_{21}}{\lambda_1} + \frac{G_{22}}{\lambda_2} \right) - \frac{G_{21}}{\lambda_1} \exp\left(-\frac{L\lambda_1 t}{HRC}\right) - \frac{G_{22}}{\lambda_2} \exp\left(-\frac{L\lambda_2 t}{HRC}\right) \right]^2, \quad (10)$$

where $G_{11} = u_{22}/u_{12}$, $G_{12} = -u_{21}/u_{11}$, $G_{21} = (-u_{21}/u_{11} + 1)G_{11}$, $G_{22} = (-u_{22}/u_{12} + 1)G_{12}$, and $F = 1/(G_{11} + G_{12})$.

The relaxation time τ is only determined by the exponential term of the above equation with λ_{min} (i.e., the smallest eigenvalue of M), therefore:

$$\tau_g = \tau_{g,0} = \tau_{g,12} = \frac{1}{\lambda_{min}} \frac{H}{L} RC = \frac{2H/L}{\lambda_{min}(1 + H/L)} \tau_{RC}. \quad (11)$$

Besides, the relaxation time of surface charge $\tau_{\sigma1} = \tau_{\sigma2} = 2R^*C/\lambda_{min} = \tau_g$.

2.2.3 | General n case

A circuit model for the n -electrode setup is shown in Figure 1C. Similar to the previous subsection, the outermost capacitor has a capacitance C , while the others have $2C$, as they mimic electrodes with electrolytes on either side. The relaxation time of HG is expressed as:

$$\tau_{g,0} = \tau_{g,12} = \dots = \tau_{g,(n-1)n} = \frac{2H/L}{(n-1)\lambda_{\min}(1+H/L)} \tau_{RC}, \quad (12)$$

$$\lambda_{\min} = \min(\text{eig}(\mathbf{M})) \text{ and } \mathbf{M} = \frac{1}{2R^*C} \begin{pmatrix} 1 + \frac{H/L}{n-1} & -1 & & & \\ -1 & 2 & -1 & & \\ & -1 & \ddots & \ddots & \\ & & \ddots & \ddots & -1 \\ & & & -1 & 2 & -1 \\ & & & & -2 & 2 \end{pmatrix}, \quad (13)$$

where \mathbf{M} is a tridiagonal matrix that is Toeplitz except for two elements ($M_{1,1}$ and $M_{n,n-1}$) and $R^* = h/(A\varepsilon_0\varepsilon_r\kappa^2D)$. The fitting formula of λ_{\min} concerning n and H/L is $\lambda_{\min} = \omega n^\beta$, where $\omega = -0.275(H/L - 3.4)^2 - 2.23$ and $\beta = 0.0075(H/L - 2.5)^2 - 2.23$, as shown in Figure S1. Interestingly, the relaxation time of surface charge τ_σ is theoretically equal to the relaxation time of HG τ_g except for the case of $n = 1$.

2.3 | Numerical method: The Poisson-Nernst-Planck and heat equations

The electrostatic potential $\phi(x,t)$, the local ionic number densities $\rho(x,t)$, and the local temperature $T(x,t)$ are modeled via the PNP and heat equations¹⁸:

$$\frac{\partial \rho_\pm}{\partial t} + \nabla \cdot \mathbf{J}_\pm = 0, \quad (14)$$

$$\mathbf{J}_\pm = -D_\pm \left(\nabla \rho_\pm + \frac{z_\pm e \rho_\pm}{k_B T} \nabla \phi + \frac{\rho_\pm Q_\pm^*}{k_B T^2} \nabla T \right), \quad (15)$$

$$\varepsilon_0 \varepsilon_r \nabla \cdot (-\nabla \phi) = eq, \quad (16)$$

$$\frac{\partial T}{\partial t} = a \nabla^2 T - \frac{e}{\rho_{m,\text{bulk}} c_p} (J_+ - J_-) \nabla \phi, \quad (17)$$

where \pm represents cation and anion, J_\pm the ionic flux, D_\pm the diffusion coefficient, z_\pm the valence of ion, Q_\pm^* single-ion heats of transport, $q = z_+ \rho_+ + z_- \rho_-$ the space charge density, $a = k / (\rho_{m,\text{bulk}} c_p)$ the thermal diffusivity, k heat conductivity, $\rho_{m,\text{bulk}}$ the mass density of the bulk phase and c_p the specific heat capacity. Equation (15) accounts for diffusion, electromigration, and thermo-diffusion, respectively. Equation (17) is the heat equation, where the left part is the rate of change of T with time, the right parts are the rate of HT and HG, respectively.

Initially, the ionic density and temperature profiles are homogeneous, and the electric potential is zero. Thereafter, at $t=0$, the electric potentials $-\psi$ and ψ are suddenly applied to the anode and cathode, respectively. In this work, we study two ideal situations for heat dissipation of supercapacitor, namely isothermal and adiabatic conditions, and other general situations. The details of initial conditions and boundary conditions are listed in Section S3.

Lian et al.²³ have proved that the PNP equations based on the stack-electrode model can be calculated over macroscopic length scales. There are as much as 5-orders-of-magnitude gap between experimental relaxation times and those predicted in simple planar electrode model. In contrast, the two timescales of charging obtained by the stack-electrode model are roughly within 1 order of magnitude from the two timescales observed in the experimental data.¹³ Given the simplicity of the stack-electrode model, the remaining discrepancies are not surprising.²³

2.4 | Parameters setup and numerical details

The current work focuses on the aqueous NaCl electrolyte at $T_0 = 298.15\text{ K}$. The ions Na^+ ($i=+$) and Cl^- ($i=-$) have valency $z_+ = -z_- = 1$. We use the following parameter set^{18,44} $D_\pm = 1.6 \times 10^{-9} \text{ m}^2/\text{s}$, $\varepsilon_r = 71$, $\rho_{\text{bulk}} = 998.3 \text{ kg/m}^3$, $c_p = 4.182 \text{ kJ}/(\text{kg}\cdot\text{K})$, $a = 1.435 \times 10^{-7} \text{ m}^2/\text{s}$, and $c_0 = 10 \text{ mol/m}^3$, while $Q_+^* = 4.05 \times 10^{-21} \text{ J}$ and $Q_-^* = 8.09 \times 10^{-22} \text{ J}$. Therefore, the Debye length $\lambda_D = \kappa^{-1}$, thermal voltage V_m and heat conductivity k are equal to $2.87 \times 10^{-9} \text{ m}$, 0.02526 V , and $0.599 \text{ W}/(\text{m}\cdot\text{K})$, respectively. The number of planar electrodes on a side n , the relative half size of electrolytic cell κL , the relative size of the electrode H/L , and the zoom factor of the flux of heat dissipation d are changeable parameters. The detailed parameter settings can be found in Table S1.

The one-dimensional governing equations and the associated initial and boundary conditions were solved using finite element methods (FEM). For FEM-models, a direct solver MUMPS (Multifrontal Massively Parallel Direct Solver) was used with a damped Newton-Raphson approach, where the relative tolerance factor is 10^{-5} . The mesh size has the smallest value at the electrode surfaces, about $0.1\lambda_D$, due to the large potential, concentration and temperature gradients, and then gradually increased away from these boundaries. The mesh was refined by reducing the element size at the electrode surfaces and the maximum element growth rate (1.2). The numerical solution process was implemented in COMSOL Multiphysics 5.3, which automatically converts the governing equations to weak formulations and corresponding weak boundary conditions.

3 | RESULTS AND DISCUSSION

3.1 | Thermal effects coupled with ion-charge transports in bulk phase and porous electrodes

In Figure 4, we present the numerical results of thermal effects coupled by multiple physical fields for the stack-electrode model of $n=4$, $H/L=1$, and $\kappa L=100$ in adiabatic conditions. For the sake of convenience, pores are named by pore1, pore2, and pore3 in turn according to the distance from the center of the bulk phase (mid, $x=0$), as shown in Figure 4A. Figure 4B-D presents the change of the dimensionless temperature rise $\Delta T/\Delta T_{\text{eq}}$, the variation of ionic concentration $(c_+ + c_- - 2c_0)/(c_{+,eq}c_{-,eq} - 2c_0)$ in the center of pores and

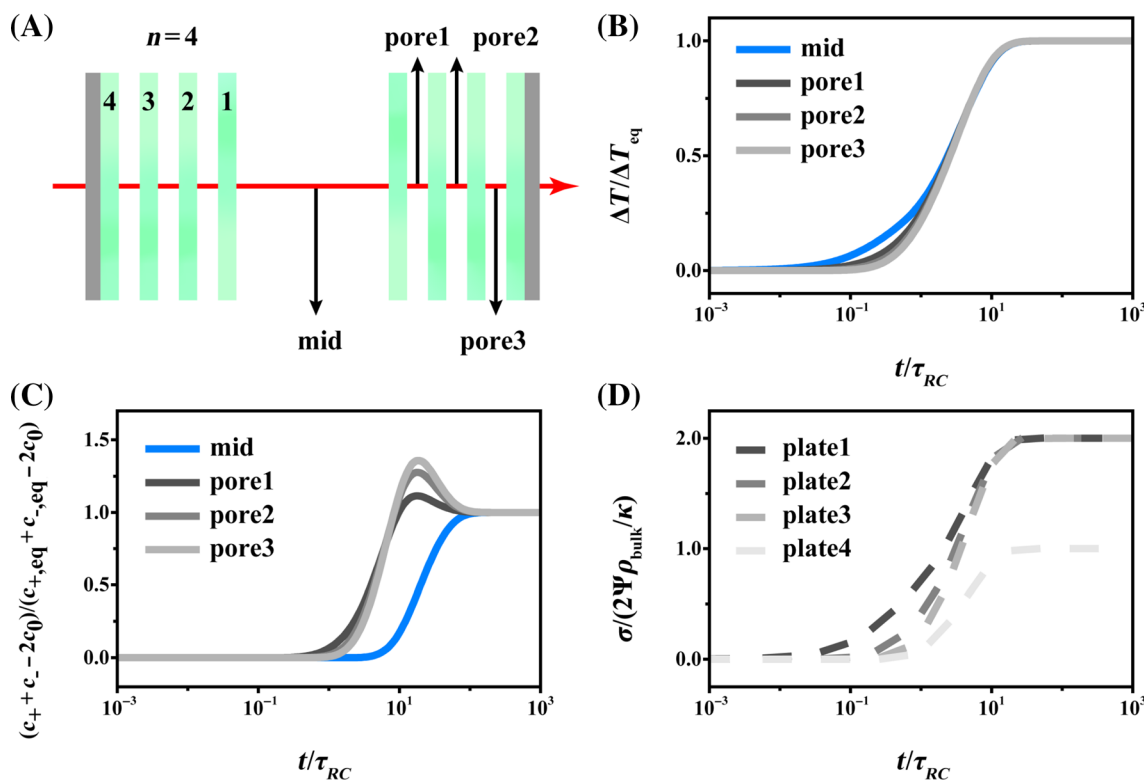


FIGURE 4 (A) The schematic diagram of the stack-electrode model of $n=4$, $H/L=1$, and $\kappa L=100$ in adiabatic conditions. The pores are named by pore1, pore2, and pore3 in order of distance from the center of the bulk phase (mid, $x=0$). The change of the dimensionless (B) temperature rise $\Delta T/\Delta T_{eq}$, (C) variation of ionic concentration $(c_+ + c_- - 2c_0)/(c_{+,eq} + c_{-,eq} - 2c_0)$ in the center of pores and bulk phase, and (D) surface charge density $\sigma/(2\Psi\rho_{bulk}/\kappa)$ on the surface of planar electrodes with dimensionless charging time t/τ_{RC}

bulk phase, and the surface charge density $\sigma/(2\Psi\rho_{bulk}/\kappa)$ on plates with dimensionless charging time t/τ_{RC} , respectively. $\Delta T=T-T_0$ and ΔT_{eq} is the adiabatic equilibrium temperature rise. τ_{RC} is the relaxation time of charging (surface charge) of planar supercapacitors derived by ECM.²³ The charging time is $10^{-5}\tau_{RC}\sim 10^5\tau_{RC}$ and system is assumed to be in equilibrium at $10^5\tau_{RC}$. Notably, the surface charge density is calculated by Gauss's law $\sigma(t)=-2\rho_{bulk}\kappa^{-2}[\partial_x\phi|_{x^+}-\partial_x\phi|_{x^-}]$. As the outermost electrodes face the electrolyte only at one side, σ_{eq} on the outermost electrodes is a factor two smaller than the surface charge density of the other electrodes.

The results show that temperature first rises in the bulk phase and then in the porous electrode, as shown in Figure 4B. Besides, the deeper the pore, the slower the local temperature starts to rise. It is understood by that the heat first generates in the bulk phase due to higher thermal resistance and current and then transfer to the porous electrode. The ions from the bulk phase can pass through the inside planar electrode with permeable zones to the outermost one, and subsequently adsorbed on the surfaces of all planar electrodes to form the EDLs. Therefore, the ionic concentration in the center of the closer pore (i.e., pore1) and surface charge density (or EDL) on the closer planar electrode (i.e., plate 1) increases (or forms) at the fastest speed, as shown in Figure 4C,D. The variation of ionic concentration in pores is caused by the ion migration and the formation of EDLs

together. Ion migration leads to higher concentration, and then the formation of EDLs decreases the concentration, finally resulting in the peaks in Figure 4C. Because the center of the bulk phase (mid) is far away from the plate than the center of pores, the variation of ionic concentration caused by forming EDLs is slower than those in pores. Besides, we find the end time of temperature rise is the same as that of surface charge relaxation while faster than that of concentration relaxation.

Although Figure 4 shows the difference of starting time and end time between pores and bulk phase in charging dynamics and thermal effect, the process of temperature rise needs to be quantitatively refined to many stages to better design the heat management system.

3.2 | The four stages of thermal effect characterized by relaxation times

For the same parameters, in Figure 5, we show the relaxation process of temperature rise for the stack-electrode model of $n=4$ in adiabatic conditions. The relaxation time τ (s) is the timescale of a variable of the system (e.g., T and c) or some dynamic processes (e.g., HG and HT) from an initial state to a steady state.

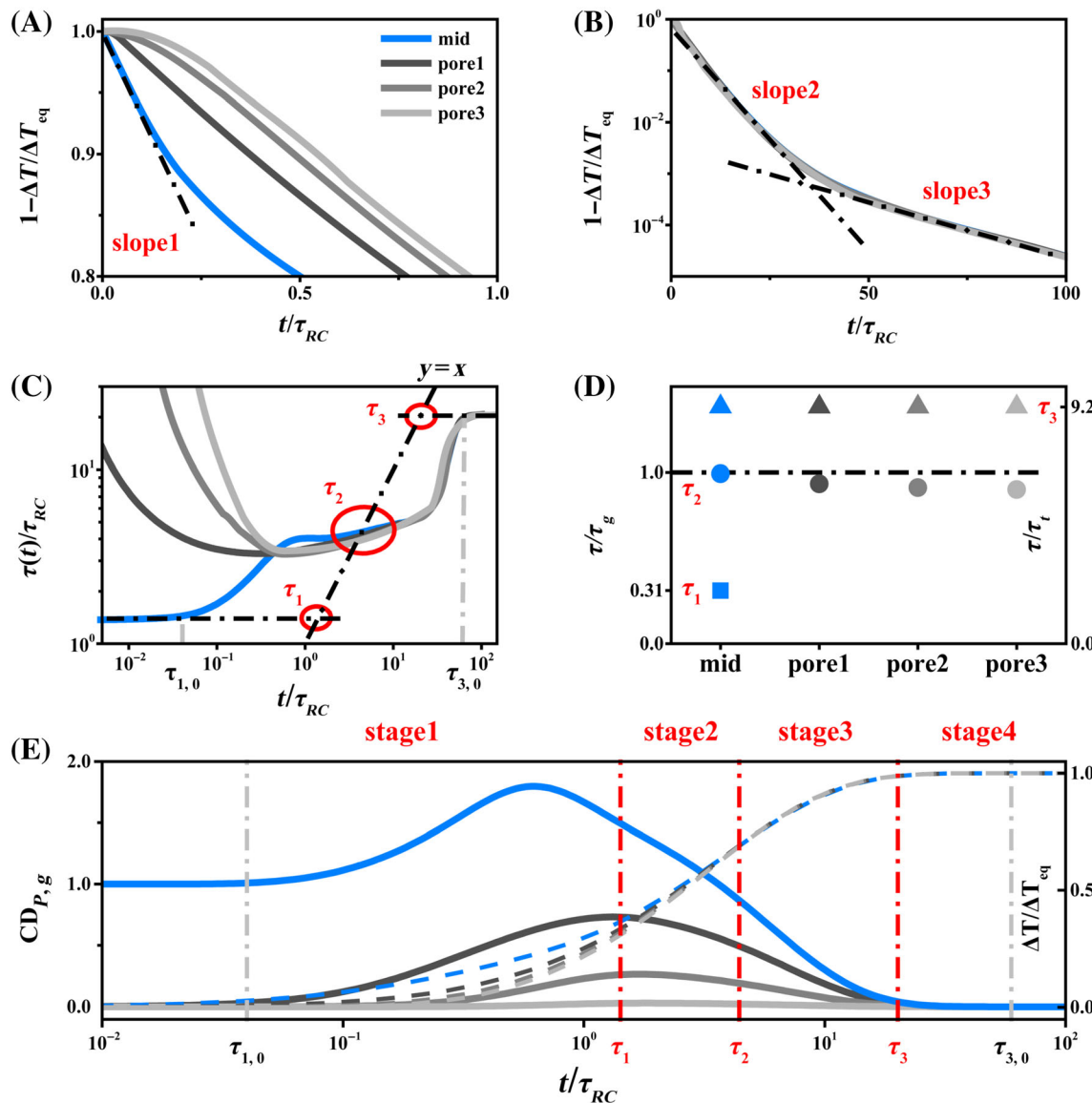


FIGURE 5 The four stages of thermal effect in the center of bulk phase (mid) and pores. (A, B) The relaxation processes of adiabatic temperature rise $1 - \Delta T / \Delta T_{eq}$ within dimensionless charging time t / τ_{RC} . (C) The time-dependent function of relaxation time $\tau(t) / \tau_{RC}$ and three numerical solutions τ_1 , τ_2 , and τ_3 . (D) The comparisons between numerical solutions and analytical solutions (τ_g and τ_t), where τ_g is the relaxation time of heat generation derived by ECM and $\tau_t = (H + L)^2 / a$ is the relaxation time of HT of planar supercapacitors.¹⁸ (E) The contribution degree (CD) of P_g to P_a (i.e., $CD_{P,g} = P_g / P_a$, solid lines), where P_g and P_a are the rate of change of temperature over time caused by heat generation and heat accumulation, respectively. The dashed line represents the change of dimensionless temperature rise $\Delta T / \Delta T_{eq}$ with t / τ_{RC}

3.2.1 | The relaxation process of adiabatic temperature rise

The relaxation processes of temperature rise $1 - \Delta T / \Delta T_{eq}$ in the center of the bulk phase (mid) and pores are plotted in Figure 5A,B. The results show that the curve characterizing the temperature relaxation in the center of the bulk phase has three steady slopes while the curves describing the cases in the pores have two ones, indicating three relaxation times (i.e., four stages) in the process of temperature rise. Figure S2 shows the relaxation processes among temperature, ionic concentration, and surface charge at three steady slope periods, respectively. During the second steady slope

period, the lines describing the temperature relaxations in both pores and bulk phase overlap with the lines describing the relaxation process of surface charge density at pore walls, indicating the second relaxation time of temperature rise relates directly to the surface charge.

3.2.2 | The numerical solutions of three relaxation times and comparation with analytical solutions

To accurately characterize different time responses during the relaxation process, according to a purely exponential temperature difference

$\Delta T = \Delta T_{\text{eq}}[1 - \exp(-t/\tau)]$ caused by HG as Equation (4), a time-dependent function $\tau(t)$ is defined as:

$$\tau(t) = -\left[\frac{d \ln(1 - \Delta T / \Delta T_{\text{eq}})}{dt}\right]^{-1}, \quad (18)$$

which intersects with $y = x$ (i.e., $\tau(t) = t$) to obtain different relaxation times τ_i . i represents different time responses. Accordingly, as shown in Figure 5C, τ_2 is the real intersection value, while τ_1 and τ_3 are the points of intersections with the extended lines of two platforms. Platform means only one process controls ΔT while curves are the results of multiple processes together. The values of the x-coordinate in which two platforms begin to change or to un-change are denoted by $\tau_{1,0}$ and $\tau_{3,0}$, respectively. Notably, three pores have no first platform since HG in pores is much less than that in the center of bulk phase at early times, due to the lower resistance and current.

To analyze analytical errors, the τ_1 and τ_2 in the center of the bulk phase and pores are nondimensionalized by τ_g derived by ECM, and τ_3 are nondimensionalized by $\tau_t = (H + L)^2/a$, as shown in Figure 5D. τ_t is the relaxation time of HT of planar supercapacitors.¹⁸ The result indicates that τ_2 approaches to the theoretical solution of HG ($\approx 1.0\tau_g$). Besides, the position of pores does not influent on τ_3 but on τ_2 .

3.2.3 | The relations between HG and HT in four stages of temperature rise

To explain the physical significance of the three relaxation times and to explore the dominant processes between the HG and HT in the four stages, the contribution degree of HG CD_g on the rates of temperature change over time P (solid lines) are plotted in Figure 5E. The formula of $CD_{P,g}$ is defined as follows:

$$CD_{P,g} = \frac{P_g}{P_a} = \frac{-\frac{e}{\rho_{m,\text{bulk}}c_p}(J_+ - J_-)\nabla\phi}{\partial T / \partial t}, \quad (19)$$

where P_g and P_a are the second part in the right (HG) and left part (heat accumulation) of Equation (17), respectively. Moreover, the contribution degree of HT $CD_{P,t}$ is equal to $100\% - CD_{P,g}$. If $CD_{P,g}$ exceeds 100% or $CD_{P,t}$ is less than zero, heat here will transfer to the surrounding. Because HT results from temperature differences produced by heterogeneous HG, we then tend to first consider the dominant process from the perspective of HG not HT.

Notably, stage1 and stage4 are segmented into two substages by $\tau_{1,0}$ and $\tau_{3,0}$ separately. At the first substage of the stage1, the $CD_{P,g}$ in the center of bulk phase is almost 100%, indicating the HG in the bulk phase is dominant for the temperature rise. In the next substage, the $CD_{P,g}$ in the pores start to increase and $CD_{P,g}$ in the center of the bulk phase exceeds 100%. Therefore, the HGs in the pores gradually affect the ΔT in the pores but the heat from the bulk phase is still the primary cause of temperature rise, and the HGs in the bulk phase are still dominant for the ΔT . At stage2, $CD_{P,g}$ in the center of the bulk phase and pores gradually decrease but the effect of HT on

temperature rise is not significant. What's more, the end time of the stage2 (i.e., τ_2) is equal to the theoretical solution of relaxation time of HG τ_g , which further proves the conclusion that stage2 is controlled by HG in the bulk phase. At stage3, HT gradually plays a more and more significant role in the temperature rise than the HG, and $CD_{P,t}$ gradually reach 99.9% (i.e., $CD_{P,g} \rightarrow 0$). The reason is that HG has reached theoretical equilibrium at the end of stage2. Finally, HT is the dominant process of stage4.

Furthermore, for this case, we find the temperature rise mainly occurs in the second substages of stage1, stage2, and stage3, as shown in the dashed line in Figure 5E. Therefore, at these stages, specific thermal management methods can be adopted to reduce the temperature rise caused by different mechanisms, such as HG or HT.

3.3 | The relationships between relaxation times and porous structures

To explore the relationships between three relaxation times and porous structures, the numerical simulations with different structural parameters (i.e., n , H/L , and κL) are performed. n is the number of planar electrodes on a side, H/L reflects the relative size of the electrode than L , and κL represents the relative half size of the electrolytic cell than λ_D . The influence of n , H/L , and κL on τ_1 , τ_2 , and τ_3 are plotted in Figure 6. The upper (white) parts of every subfigure show the change of the numerical solutions of three relaxation times with structural parameters. In the lower (gray) parts of every subfigure, the numerical solutions of three relaxation times are divided by the theoretical solutions of relaxation time of HG derived by ECM (i.e., τ_g) or those of HT in planar electrode (i.e., τ_t). If all points are on a horizontal line, this indicates that the formula of τ_g or τ_t has already taken the corresponding structural parameter into account, while it should be modified if not on a horizontal line.

3.3.1 | The first relaxation time τ_1

We find that both n and H/L have a great influence on τ_1/τ_{RC} except for κL because n and H/L can change the relative size of resistance between the bulk phase and one pore (i.e., L/h). If the resistances of pores are smaller (i.e., greater n or less H/L causing smaller h), HG in the bulk phase will dominate the temperature rise process for a longer time, and thus the start time of stage2 is delayed (i.e., greater τ_1/τ_{RC}). The τ_1/τ_g of every n and κL are almost equivalent while τ_1/τ_g gradually increase with the decrease of H/L . The fitted formula between τ_1/τ_g and H/L is $0.16(H/L)^2 - 0.6(H/L) + 0.742$, as shown in Figure S3a. Therefore, the modified formula of τ_1 is as follows:

$$\begin{aligned} \tau_1 &= [0.16(H/L)^2 - 0.6(H/L) + 0.742]\tau_g \\ &\approx \frac{0.3[(H/L)^2 - 4H/L + 5](H/L)}{(n-1)\lambda_{\min}(\kappa L)D} \\ &= \frac{0.3[(H/L-2)^2 + 1](H/L)}{(n-1)\lambda_{\min}(\kappa L)D}. \end{aligned} \quad (20)$$

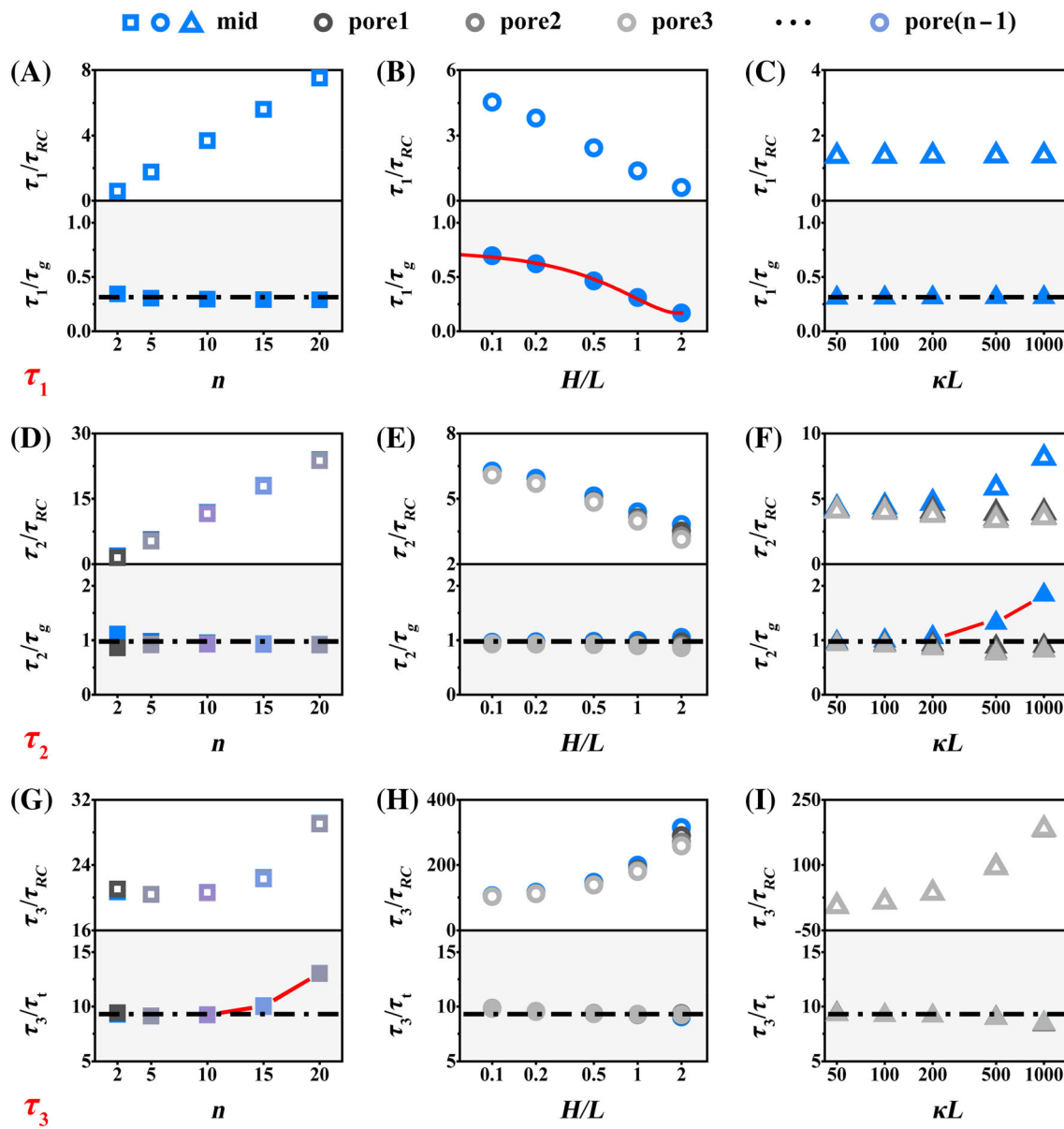


FIGURE 6 The influence of structural parameters on three relaxation times τ_1 , τ_2 , and τ_3 (upper part of every subfigure), and the comparation between numerical solutions and analytical solutions (lower part of every subfigure) in the center of the bulk phase and pores in adiabatic conditions. (A, D, G) $n = \{2, 5, 10, 15, 20\}$, (B, E, H) $H/L = \{0.1, 0.2, 0.5, 1, 2\}$, and (C, F, I) $\kappa L = \{50, 100, 200, 500, 1000\}$. The default values of these parameters are $n = 4$, $H/L = 1$, and $\kappa L = 100$ unless adjusting one of them

Notably, $\tau_{1,H/L=0}/\tau_{1,n=1} = 1.06 \approx 1$, where $\tau_{1,H/L=0}$ is the value of the fitted curve when $H/L=0$ and $\tau_{1,n=1}$ is the first relaxation time calculated from the simulation of planar supercapacitors. This proves the stack-electrode model can returns to planar electrode model when $H/L \rightarrow 0$. The error is due to the overlap of EDLs caused by the decrease of pore diameter $h = [(H/L)(\kappa L)]/[\kappa(n-1)] \leq 2\lambda_D$ with the reduction of H/L . What's more, this also supports the description that the stage1 is mainly controlled by the HG in the bulk phase rather than in the pores or in both.

3.3.2 | The second relaxation time τ_2

For τ_2/τ_{RC} , the trends with n , H/L , and κL are similar to those of τ_1/τ_{RC} . The great n and small H/L result in relatively small pore diameter h/L and greater heat-transfer resistance, causing difficulty of HT from the bulk phase to the outmost pore (i.e., greater τ_2/τ_{RC}). Interestingly, τ_2/τ_{RC} in the center of bulk phase sharply increases as the size of the system κL increases while those in the pores stay the same, as shown in Figure 6F. The abnormal rise can be explained by the ratio of the timescales of HG to HT, namely:

$$\begin{aligned}\frac{\tau_g}{\tau_t} &= \left[\frac{2H/L}{(n-1)\lambda_{\min}(1+H/L)} \tau_{RC} \right] / \left[\frac{(H+1)^2}{a} \right] \\ &= \frac{2a}{D} \frac{H/L}{\lambda_{\min}(n-1)(\kappa L)}. \end{aligned} \quad (21)$$

The τ_g/τ_t for $\kappa L = \{50, 100, 200, 500, 1000\}$ equal to $\{15.8, 7.9, 4.0, 1.6, 0.8\}$. If $\tau_g/\tau_t \gg 1$ (i.e., $\kappa L = 50, 100, 200$), the boundary of HG and HT is clear, and the values of τ_2/τ_{RC} in the center of bulk phase and pores are closer. However, if $\tau_g/\tau_t \rightarrow 1$ (i.e., $\kappa L = 500$) and even $\tau_g/\tau_t < 1$ (i.e., $\kappa L = 1000$), the boundary will vanish and HT will significantly affect the thermal effect in stage2, which causes stage2 to be divided into two substages by $\tau_{2,0}$ like stage1 and stage4 (see Section S4 for details). The fitted formula between τ_2 and κL is:

$$\begin{aligned}\tau_{2,mid} &= \left\{ 3 \times 10^{-7} [(\kappa L)^2 + 2000(\kappa L)] + 0.928 \right\} \tau_g \\ &= \frac{\left\{ 6 \times 10^{-7} [(\kappa L)^2 + 2000(\kappa L)] + 0.928 \right\} (H/L)}{(n-1)\lambda_{\min} + (\kappa L)D} \\ &= \frac{[6 \times 10^{-7} (\kappa L + 1000)^2 + 0.328] (H/L)}{(n-1)\lambda_{\min}(\kappa L)D}, \end{aligned} \quad (22)$$

$$\tau_{2,pores} = \tau_g = \frac{2(H/L)}{(n-1)\lambda_{\min}(\kappa L)D}. \quad (23)$$

The detailed fitting results are shown in Figure S3b.

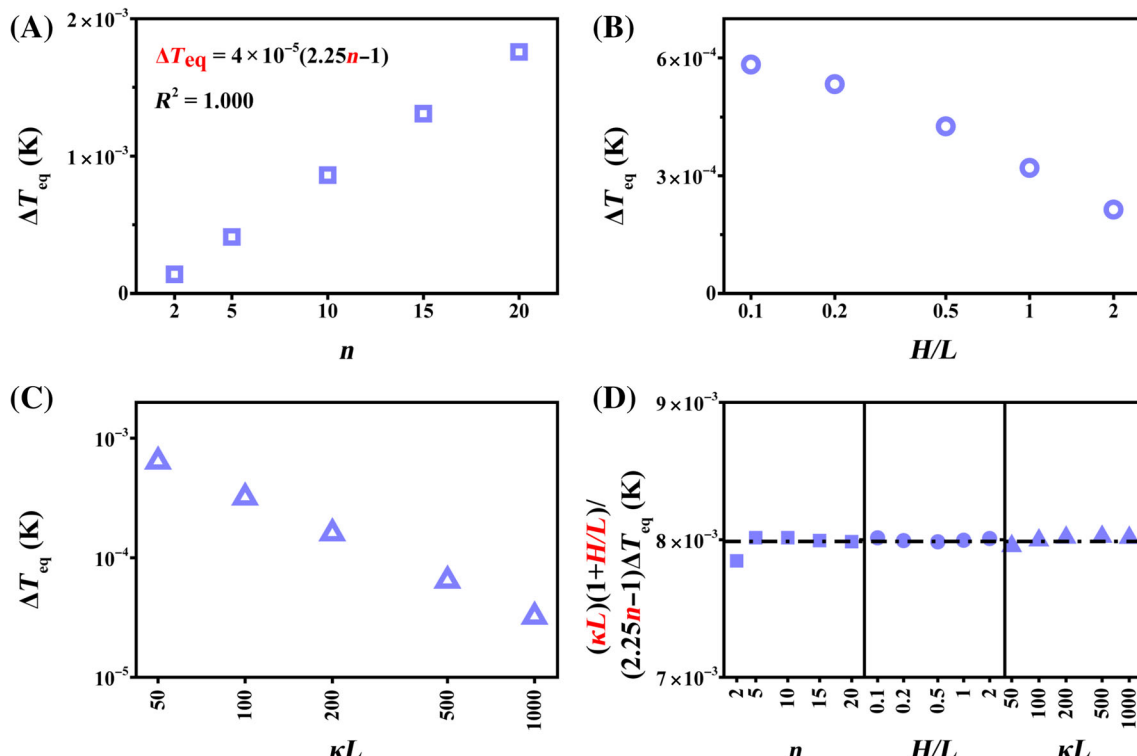


FIGURE 7 The adiabatic temperature rise at equilibrium $\Delta T_{eq} = T_{eq} - T_0$ for different (A) n , (B) H/L , and (C) κ . (D) The changes of temperature $(\kappa L)(1+H/L)/(2.25n-1)\Delta T_{eq}$ with different structural parameters

3.3.3 | The third relaxation time τ_3

For stage3, τ_3/τ_{RC} almost exponentially grows with the increase of n , H/L , and κL . The stage3 is controlled by HT, which makes the temperature distribution homogenous. The greater absolute size of supercapacitors (i.e., $H+L$) and larger temperature difference between the bulk phase and pores $|T_{bulk} - T_{pore}|$ cause a longer time of HT from the bulk phase to the outermost pores. Greater H/L and κL result in the bigger $H+L$. Meanwhile, greater n leads to greater $|T_{bulk} - T_{pore}|$ due to lesser heat produced in pores than in the bulk phase under greater n . Only the curve between τ_3/τ_t and n are not on a horizontal line because $\tau_t = \kappa(H+L)/a$ is not related with n . The relationship between τ_3 and n satisfies the following formula:

$$\begin{aligned}\tau_3 &= (0.0014n^3 - 0.0225n^2 + 0.0882n + 9.147)\tau_t \\ &\approx \frac{[0.0014n(n+8)^2 + 9.147](\kappa L)^2(1+H/L)^2}{\kappa^2 a}. \end{aligned} \quad (24)$$

See Figure S3c for details.

3.4 | The relationships between adiabatic temperature rise at equilibrium and porous structures

The adiabatic temperature rise at equilibrium $\Delta T_{eq} = T_{eq} - T_0$ is another important indicator to quantify the thermal effect. In

Figure 7, the changes of ΔT_{eq} with structural parameters are plotted. With the decrease of H/L and κL and the increase of n , ΔT_{eq} increases almost linearly, which can be explained by Equation (4). When charging time is infinite (i.e., $t = 10^5 \tau_{RC}$ in this work), the system reaches equilibrium and $[1 - \exp(-4t/(RC))] \rightarrow 1$. Therefore, $\Delta T_{eq} = C/[(\kappa L)(1 + H/L)]$, where C is a constant independent of κL and H/L . Because Equation (4) is not suitable for the case of $n > 1$, and the analytical solution is complicated, the relation between ΔT_{eq} and n is fitted as $\Delta T_{eq} \sim 2.25n - 1$. Therefore, ΔT_{eq} with different structural parameters can be modified as:

$$\Delta T_{eq} = \left(\frac{\epsilon \kappa^2 \Psi^2}{2\rho_m \text{bulk} C_P} \right) \frac{2.25n - 1}{(\kappa L)(1 + H/L)}. \quad (25)$$

Finally, to verify the formula, the temperature $[(\kappa L)(1 + H/L)/(2.25n - 1)]\Delta T_{eq}$ with different structural parameters is shown in Figure 7D. We can find that all points are at the same height, which demonstrates that Equation (25) can predict the adiabatic temperature rise for different structures.

3.5 | The relationships between temperature rise at the end of every stage and porous structures

Because every stage is controlled by one of HG and HT or both, the temperature rises at the end of every stage and those during every stage are important for comparison of the contribution of HG and HT

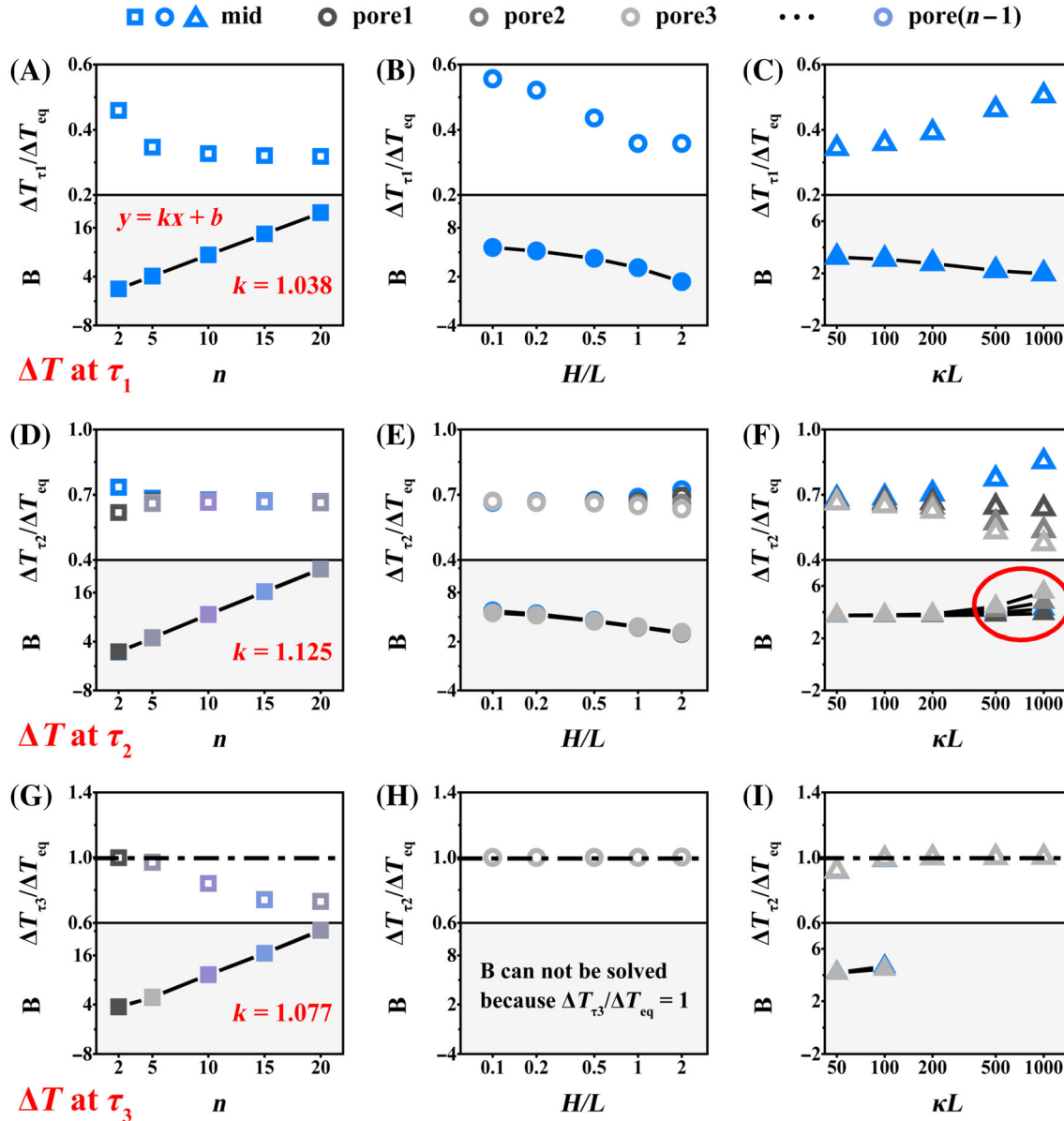


FIGURE 8 The influence of structural parameters on ΔT_{τ_i} (i.e., ΔT at τ_1 , τ_2 , and τ_3) (upper part of every subfigure), and a factor B (lower part of every subfigure) in the center of the bulk phase and pores in adiabatic conditions, where B is obtained by $\Delta T_{\tau_i}/\Delta T_{eq} = 1 - \exp[-\tau_i/(\tau_{RC}B)]$. (A, D, G) $n = \{2, 5, 10, 15, 20\}$, (B, E, H) $H/L = \{0.1, 0.2, 0.5, 1, 2\}$, and (C, F, I) $\kappa L = \{50, 100, 200, 500, 1000\}$. The default values of these parameters are $n = 4$, $H/L = 1$, and $\kappa L = 100$ unless adjusting one of them

on ΔT_{eq} . Therefore, in the upper (white) parts of Figure 8, the influences of structural parameters on $\Delta T/\Delta T_{\text{eq}}$ at τ_1 , τ_2 , and τ_3 (i.e., ΔT_{τ_i}) are plotted, which are dimensionless temperature rise at the end of stage1, stage2, and stage3, respectively. Notably, the temperature rises at the end of stage4 are the adiabatic temperature rise at equilibrium ΔT_{eq} . The results show that $\Delta T/\Delta T_{\text{eq}}$ at τ_2 are near 0.7 for any n , H/L , and κL except for the cases when $\tau_g/\tau_t \rightarrow 1$ or $\tau_g/\tau_t < 1$. Besides, $\Delta T_{\tau_3}/\Delta T_{\text{eq}} \neq 1$ indicates that temperature has not reached equilibrium in the end of stage3 and stage4 controlled by HT is significant for the cases, as shown in the upper part of Figure 8G.

The formulas for directly fitting $\Delta T/\Delta T_{\text{eq}}$ and structural parameters are complicated. In addition, for the same structural parameters, the fitting formulas under different τ_i is not same. Inspired by Equation (4) describing the temperature rise only caused by HG, we assume $\Delta T/\Delta T_{\text{eq}}$ at τ_1 , τ_2 , and τ_3 satisfy the formula:

$$\frac{\Delta T_{\tau_i}}{\Delta T_{\text{eq}}} = 1 - \exp\left(-\frac{1}{B} \frac{\tau_i}{\tau_{RC}}\right), \quad (26)$$

$$B = -\frac{\tau_i}{\tau_{RC}} \cdot \left[\ln\left(1 - \frac{\Delta T_{\tau_i}}{\Delta T_{\text{eq}}}\right) \right]^{-1}, \quad (27)$$

where B is a correction factor and $i = \{1, 2, 3\}$. The changes of B with n , H/L , and κL are shown in the lower (gray) parts of every subfigure in Figure 8. Interestingly, the value of B with the same structural parameter under different τ is similar. For example, the slope of all fitted lines between n and B under different τ_i approaches 1. This interesting phenomenon demonstrates B is less affected by τ_i , but more by structural parameters. Since $\tau_g/\tau_t \rightarrow 1$ and even $\tau_g/\tau_t < 1$ for $\kappa L = \{500, 1000\}$, the curves of B in the center of the bulk phase and pores cannot be overlapped, as shown in Figure 8F.

The contribution degree of temperature rises during every stage on total temperature rise $CD_{\Delta T/\Delta T_{\text{eq}}}$ is defined as:

$$\begin{aligned} CD_{\Delta T/\Delta T_{\text{eq}}}^{\text{stage1}} &= \Delta T_{\tau_1}/\Delta T_{\text{eq}}, \\ CD_{\Delta T/\Delta T_{\text{eq}}}^{\text{stage2}} &= (\Delta T_{\tau_2} - \Delta T_{\tau_1})/\Delta T_{\text{eq}}, \\ CD_{\Delta T/\Delta T_{\text{eq}}}^{\text{stage3}} &= (\Delta T_{\tau_3} - \Delta T_{\tau_2})/\Delta T_{\text{eq}}, \\ CD_{\Delta T/\Delta T_{\text{eq}}}^{\text{stage4}} &= 1 - \Delta T_{\tau_3}/\Delta T_{\text{eq}}. \end{aligned} \quad (28)$$

According to Equations (20)–(27), the formulas of $CD_{\Delta T/\Delta T_{\text{eq}}}$ of every stage can be easily obtained. The $CD_{\Delta T/\Delta T_{\text{eq}}}$ in the center of bulk phase at different n , H/L , and κL are shown in Figure S6. Generally, temperature rise during stage1 and stage4 make the largest and smallest contributions on ΔT_{eq} in the center of the bulk phase, respectively.

3.6 | The influence of heat dissipation on thermal effect

Because supercapacitors typically operate under heat dissipation in practical applications, we also study relaxation times and temperature

rise at different intensity of heat dissipation ($d \neq 0$) in Section S5. The numerical results of heat dissipation still show four stages during temperature variation and HT is replaced by heat dissipation at stage3 and stage4. What's more, three relaxation times and maximum temperature rise decrease with the increase of heat dissipation intensity d .

4 | CONCLUSION

In summary, we systematically studied the thermal effect in the supercapacitors with porous electrodes by the one-dimension stack-electrode model. The analytical solution from the ECM, and the numerical simulations from the PNP and heat equations are combined, to derive the formulas of three relaxation times of temperature rise (i.e., τ_1 , τ_2 , and τ_3) for different structural parameters and operating conditions. According to the three relaxation times, the temperature rise process can be divided into four stages: HG controlled by the bulk phase (stage1), HG controlled by the bulk phase and pores together (stage2), HG as well as HT together (stage3), and HT (stage4). Furthermore, the structure–property relationships of adiabatic temperature rise at equilibrium ΔT_{eq} , and temperature rise at the end of every stage ΔT_{τ_i} are obtained by modifying analytical solutions. The ratio of them $\Delta T_{\tau_i}/\Delta T_{\text{eq}}$ is examined to compare the contribution of HG and HT on temperature rise. Therefore, we can use these simple formulas with clear physical meanings to evaluate the influence of structural parameters and operating conditions, especially the intensity of heat dissipation on thermal effect: (1) when (and how long) every stage of temperature rise starts (and lasts); (2) what mechanism causes temperature rise of every stage (i.e., HG or HT in the bulk phase or pores); and (3) how important the temperature rise of every stage ΔT_{τ_i} contributes to ΔT_{eq} . Finally, an intelligent thermal management system can be rationally designed to reduce the temperature rise by different methods during different stages based on these formulas. Therefore, this work may provide theoretical guidance for the design of thermal management system of supercapacitors, even other energy storage devices.

In the future, more structural parameters of electrodes, such as pore-size distribution and micropores,²¹ should be considered in the stack-electrode model to achieve more realistic materials simulations. Besides, reversible heat, which has a great influence on the thermal effect in pores, should be also considered.^{17,45}

AUTHOR CONTRIBUTIONS

Pan Huang: Conceptualization (supporting); data curation (lead); formal analysis (lead); investigation (lead); methodology (equal); software (lead); validation (lead); visualization (lead); writing – original draft (lead); writing – review and editing (lead). **Haolan Tao:** Methodology (equal); writing – original draft (supporting); writing – review and editing (supporting). **Jie Yang:** Writing – original draft (supporting); writing – review and editing (supporting). **Cheng Lian:** Conceptualization (lead); funding acquisition (equal); methodology (equal); project administration (equal); resources (equal); supervision (lead);

writing – original draft (supporting); writing – review and editing (supporting). **Honglai Liu:** Funding acquisition (equal); project administration (equal); resources (equal); supervision (supporting).

ACKNOWLEDGMENTS

This work was sponsored by the National Natural Science Foundation of China (No. 91834301, 22078088), the National Natural Science Foundation of China for Innovative Research Groups (No. 51621002), the Shanghai Rising-Star Program (No. 21QA1401900), and Jiangsu Engineering Laboratory of New Materials for Sewage Treatment and Recycling. We kindly thank Réne van Roij for his helpful discussions.

CONFLICT OF INTEREST

The authors declare no competing interests.

DATA AVAILABILITY STATEMENT

The simulated data presented in this work are available from the corresponding authors on reasonable request.

ORCID

Cheng Lian  <https://orcid.org/0000-0002-9016-832X>

REFERENCES

1. Simon P, Gogotsi Y. Materials for electrochemical capacitors. *Nat Mater.* 2008;7(11):845-854.
2. Chmiola J, Largeot C, Taberna PL, Simon P, Gogotsi Y. Monolithic carbide-derived carbon films for micro-supercapacitors. *Science.* 2010;328(5977):480-483.
3. Yang Z, Zhang J, Kintner-Meyer MCW, et al. Electrochemical energy storage for green grid. *Chem Rev.* 2011;111(5):3577-3613.
4. Kou L, Huang T, Zheng B, et al. Coaxial wet-spun yarn supercapacitors for high-energy density and safe wearable electronics. *Nat Commun.* 2014;5(1):3754.
5. Wang Q, Yan J, Fan Z. Carbon materials for high volumetric performance supercapacitors: design, progress, challenges and opportunities. *Energ Environ Sci.* 2016;9(3):729-762.
6. Carignano MG, Costa-Castelló R, Roda V, Nigro NM, Junco S, Feroldi D. Energy management strategy for fuel cell-supercapacitor hybrid vehicles based on prediction of energy demand. *J Power Sources.* 2017;360:419-433.
7. Gualous H, Louahlia-Gualous H, Gallay R, Miraoui A. Supercapacitor thermal modeling and characterization in transient state for industrial applications. *IEEE Trans Ind Appl.* 2009;45(3):1035-1044.
8. Gualous H, Louahlia H, Gallay R. Supercapacitor characterization and thermal modelling with reversible and irreversible heat effect. *IEEE Trans Power Electron.* 2011;26(11):3402-3409.
9. Kötz R, Hahn M, Gallay R. Temperature behavior and impedance fundamentals of supercapacitors. *J Power Sources.* 2006;154(2):550-555.
10. Guillet P, Scudeller Y, Brousse T. Multi-level reduced-order thermal modeling of electrochemical capacitors. *J Power Sources.* 2006;157(1):630-640.
11. Al Sakka M, Gualous H, Van Mierlo J, Culcu H. Thermal modeling and heat management of supercapacitor modules for vehicle applications. *J Power Sources.* 2009;194(2):581-587.
12. Munteşari O, Lau J, Krishnan A, Dunn B, Pilon L. Isothermal calorimeter for measurements of time-dependent heat generation rate in individual supercapacitor electrodes. *J Power Sources.* 2018;374:257-268.
13. Janssen M, Griffioen E, Biesheuvel PM, van Roij R, Erné B. Coulometry and calorimetry of electric double layer formation in porous electrodes. *Phys Rev Lett.* 2017;119(16):166002.
14. Merlet C, Rotenberg B, Madden PA, et al. On the molecular origin of supercapacitance in nanoporous carbon electrodes. *Nat Mater.* 2012;11(4):306-310.
15. Merlet C, Péan C, Rotenberg B, et al. Highly confined ions store charge more efficiently in supercapacitors. *Nat Commun.* 2013;4(1):2701.
16. d'Entremont A, Pilon L. First-principles thermal modeling of electric double layer capacitors under constant-current cycling. *J Power Sources.* 2014;246:887-898.
17. d'Entremont AL, Pilon L. First-principles thermal modeling of hybrid pseudocapacitors under galvanostatic cycling. *J Power Sources.* 2016;335:172-188.
18. Janssen M, Bier M. Transient response of an electrolyte to a thermal quench. *Phys Rev E.* 2019;99(4):042136.
19. Porada S, Hamelers HVM, Biesheuvel PM. Electrostatic cooling at electrolyte-electrolyte junctions. *Phys Rev Res.* 2019;1(3):033195.
20. Tao H, Chen G, Lian C, Liu H, Coppens MO. Multiscale modeling of ion transport in porous electrodes. *AIChE J.* 2022;68(4):e17571.
21. Singh K, Bouwmeester HJM, de Smet LCPM, Bazant MZ, Biesheuvel PM. Theory of water desalination with intercalation materials. *Phys Rev Appl.* 2018;9(6):064036.
22. Tao H, Lin S, Lian C, Li C, Liu H. Microscopic insights into the ion transport in graphene-based membranes with different interlayer spacing distributions. *Chem Eng Sci.* 2020;212:115354.
23. Lian C, Janssen M, Liu H, van Roij R. Blessing and curse: how a supercapacitor's large capacitance causes its slow charging. *Phys Rev Lett.* 2020;124(7):076001.
24. Noh C, Jung Y. Understanding the charging dynamics of an ionic liquid electric double layer capacitor via molecular dynamics simulations. *Phys Chem Chem Phys.* 2019;21(13):6790-6800.
25. Kondrat S, Wu P, Qiao R, Kornyshev AA. Accelerating charging dynamics in subnanometre pores. *Nat Mater.* 2014;13(4):387-393.
26. Fletcher S, Black VJ, Kirkpatrick I. A universal equivalent circuit for carbon-based supercapacitors. *J Solid State Electrochem.* 2014;18(5):1377-1387.
27. Parvini Y, Siegel JB, Stefanopoulou AG, Vahidi A. Supercapacitor electrical and thermal modeling, identification, and validation for a wide range of temperature and power applications. *IEEE Trans Ind Electron.* 2016;63(3):1574-1585.
28. Tao H, Lian C, Liu H. Multiscale modeling of electrolytes in porous electrode: from equilibrium structure to non-equilibrium transport. *Green Energy Environ.* 2020;5(3):303-321.
29. Xu H, Zhu J, Finegan DP, et al. Guiding the design of heterogeneous electrode microstructures for Li-ion batteries: microscopic imaging, predictive modeling, and machine learning. *Adv Energy Mater.* 2021;11(19):2003908.
30. Prehal C, Koczwara C, Jäckel N, et al. Quantification of ion confinement and desolvation in nanoporous carbon supercapacitors with modelling and in situ X-ray scattering. *Nat Energy.* 2017;2(3):16215.
31. Doyle M, Newman J. The use of mathematical modeling in the design of lithium/polymer battery systems. *Electrochim Acta.* 1995;40(13):2191-2196.
32. Fuller TF, Doyle M, Newman J. Simulation and optimization of the dual lithium ion insertion cell. *J Electrochem Soc.* 1994;141(1):1-10.
33. Chadha TS, Suthar B, Rife D, Subramanian VR, Biswas P. Model based analysis of one-dimensional oriented lithium-ion battery electrodes. *J Electrochem Soc.* 2017;164(11):E3114-E3121.
34. Du J, Tao H, Chen Y, Yuan X, Lian C, Liu H. Thermal management of air-cooling lithium-ion battery pack. *Chin Phys Lett.* 2021;38(11):118201.

35. Biesheuvel PM, Fu Y, Bazant MZ. Electrochemistry and capacitive charging of porous electrodes in asymmetric multicomponent electrolytes. *Russ J Electrochem.* 2012;48(6):580-592.
36. He F, Biesheuvel PM, Bazant MZ, Hatton TA. Theory of water treatment by capacitive deionization with redox active porous electrodes. *Water Res.* 2018;132:282-291.
37. Jiang J, Cao D, Jiang D-E, Wu J. Time-dependent density functional theory for ion diffusion in electrochemical systems. *J Phys Condens Matter.* 2014;26(28):284102.
38. Rica RA, Ziano R, Salerno D, Mantegazza F, Bazant MZ, Brogioli D. Electro-diffusion of ions in porous electrodes for capacitive extraction of renewable energy from salinity differences. *Electrochim Acta.* 2013; 92:304-314.
39. Biesheuvel PM, Fu Y, Bazant MZ. Diffuse charge and Faradaic reactions in porous electrodes. *Phys Rev E.* 2011;83(6):061507.
40. Huang J. Generalization of porous electrode theory for noninteger dimensional space. *J Phys Chem C.* 2018;122(1):557-565.
41. Qin X, Cai J, Xu P, Dai S, Gan Q. A fractal model of effective thermal conductivity for porous media with various liquid saturation. *Int J Heat Mass Transf.* 2019;128:1149-1156.
42. Lin Y, Lian C, Unibaso Berrueta M, Liu H, van Roij R. Microscopic model for cyclic voltammetry of porous electrodes. *Phys Rev Lett.* 2022;128:206001.
43. Hernández-García KM, Cercado B, Rodríguez FA, Rivera FF, Rivero EP. Modeling 3D current and potential distribution in a microbial electrolysis cell with augmented anode surface and non-ideal flow pattern. *Biochem Eng J.* 2020;162:107714.
44. Nightingale ER. Phenomenological theory of ion solvation. Effective radii of hydrated ions. *J Phys Chem.* 1959;63(9):1381-1387.
45. d'Entremont AL, Pilon L. Thermal effects of asymmetric electrolytes in electric double layer capacitors. *J Power Sources.* 2015;273: 196-209.

SUPPORTING INFORMATION

Additional supporting information may be found in the online version of the article at the publisher's website.

How to cite this article: Huang P, Tao H, Yang J, Lian C, Liu H. Four stages of thermal effect coupled with ion-charge transports during the charging process of porous electrodes. *AIChE J.* 2022;e17790. doi:[10.1002/aic.17790](https://doi.org/10.1002/aic.17790)